*R*esearch in
*A*stronomy and
*A*strophysics

# The relative calibration of radial velocity for LAMOST medium resolution stellar spectra

Jian-Ping Xiong[1,2], Bo Zhang[3], Chao Liu[4,2]⋆, Jiao Li[4,5], Yong-Heng Zhao[1,2,7] and Yong-Hui Hou[6,7]

[1] Key Laboratory of Optical Astronomy, National Astronomical Observatories, Chinese Academy of Sciences, Beijing 100101, China

[2] University of Chinese Academy of Sciences, Beijing 100049, China

[3] Department of Astronomy, Beijing Normal University, Beijing 100875, China

[4] Key Laboratory of Space Astronomy and Technology, National Astronomical Observatories, Chinese Academy of Sciences, Beijing 100101 China; *liuchao@nao.cas.cn*

[5] Yunnan Observatories, Chinese Academy of Sciences, Kunming 650011, China

[6] Nanjing Institute of Astronomical Optics & Technology, National Astronomical Observatories, Chinese Academy of Sciences, Nanjing 210042, China

[7] School of Astronomy and Space Science, University of Chinese Academy of Sciences, Beijing 100049, China

**Abstract** The Large Sky Area Multi-Object Fiber Spectroscopic Telescope (LAMOST) started a median-resolution spectroscopic (MRS, $R\sim7500$) survey since October 2018. The main scientific goals of MRS, including binary stars, pulsators and other variable stars, were launched with a time-domain spectroscopic survey. However, the systematic errors, including the bias induced from wavelength calibration and the systematic difference between different spectrographs, have to be carefully considered during radial velocity measurement. In this work, we provide a technique to correct the systematics in the wavelength calibration based on the relative radial velocity measurements from LAMOST MRS spectra. We show that, for the stars with multi-epoch spectra, the systematic bias which is induced from the exposures on different nights can be corrected well for LAMOST MRS in each spectrograph. In addition, the precision of radial velocity zero-point of multi-epoch time-domain observations reaches below $0.5\,\mathrm{km\,s^{-1}}$. As a by-product, we also give the constant star candidates⋆⋆, which can be the secondary radial-velocity standard star candidates of LAMOST MRS time-domain surveys.

**Key words:** methods: data analysis — techniques: radial velocities — stars: statistics — catalogs — surveys

## 1 INTRODUCTION

Over the past years, large spectroscopic surveys, such as RAVE (Steinmetz et al. 2006, 2020), SDSS/SEGUE (Yanny et al. 2009), LAMOST (Cui et al. 2012; Deng et al. 2012; Zhao et al. 2012; Luo et al. 2015), APOGEE (Majewski et al. 2017), GALAH (De Silva et al. 2015) and Gaia (Gilmore et al. 2012; Katz et al. 2004; Cropper et al. 2018) have yielded a large number of stellar spectra that

can be used to understand galaxy formation and evolution (Gao et al. 2015; Mesa et al. 2021). As a fundamental property that can be measured directly from stellar spectra, radial velocity (RV) is the basic ingredient for many studies, such as study of the properties of a binary (Gao et al. 2014; Tian et al. 2018; Sana et al. 2012, 2013), Milky Way dynamics (Tian et al. 2020), asteroseismology (Arentoft et al. 2019) and even searching for black holes (Liu et al. 2019).

For large spectroscopic surveys, the RV uncertainty of low-resolution spectra is larger than $3 - 5\,\mathrm{km\,s^{-1}}$ for SEGUE in $R\sim1800$ (Yanny et al. 2009), and around $3 - 5\,\mathrm{km\,s^{-1}}$ for LAMOST in $R\sim1800$ (Wu et al. 2014). Such

---

⋆ corresponding author

⋆⋆ The constant stars here in this work represent the stars with low radial velocity variations. They are not necessarily absolutely constant stars, but may not exhibit significant radial velocity variation during the time-domain survey.

precision is very useful in Milky Way studies, however, it is not enough in lots of studies of stars and stellar systems, e.g., the internal dynamics of open clusters (with RV dispersion of $< 1\,\mathrm{km\,s^{-1}}$, Pang et al. (2021a)), the disruption process of open clusters (with RV dispersion around $1 - 3\,\mathrm{km\,s^{-1}}$, Pang et al. 2021b), binary stars with a larger range of period and low-amplitude variables. The precision of RV is required down to $< 1\,\mathrm{km\,s^{-1}}$ for these studies. This is essentially the motivation for the LAMOST medium-resolution spectroscopic (MRS) survey with $R \sim 7500$.

Since October 2018, LAMOST started the 5-year MRS survey (Liu et al. 2020). A large amount of medium resolution stellar spectra will be obtained. It provides an opportunity to study the kinematics and dynamics of stars more accurately. For the LAMOST MRS survey, Wang et al. (2019) derived RV with the cross-correlation method, and the precision achieves $1.36\,\mathrm{km\,s^{-1}}$, $1.08\,\mathrm{km\,s^{-1}}$ and $0.91\,\mathrm{km\,s^{-1}}$ for spectra at the single-to-noise ratio (SNR) of 10, 20 and 50, respectively, after being calibrated with the RV standard stars (Huang et al. 2018).

However, there are a few issues that need to be addressed well. One is that the wavelength calibration of the spectra of LAMOST demonstrates that it may shift by a few $\mathrm{km\,s^{-1}}$ during one night, which is likely due to the variation of the environments of the spectrographs (Zhang Hao-Tong, priv. comm.). The systematic shift between different exposures may severely affect the orbital parameter estimates in binary studies. In the meantime, because LAMOST contains 16 spectrographs, one star can be observed by different spectrographs on different nights, depending on the specific fiber assignment strategy. This may introduce another systematic difference in time-domain spectra, due to the systematically different wavelength calibrations between different spectrographs. It means that the instability of the wavelength calibration may induce a large fraction of systematic errors in the uncertainty of RV.

It is noted that many studies, e.g. the pulsation of stars, the binarities, etc., do not require absolute RVs, but only relative ones. Specifically, at time $t$, a star has a directly measured RV such as $v_t = v_0 + \Delta v_t + \epsilon$, where $v_0$ is the systematic RV of the star, $\Delta v_t$ is the term of possible variation if the star is a pulsator or a companion in a binary system and $\epsilon$ is the measurement uncertainty. To understand the pulsational process or the parameters of the orbits of a binary system using a series of time-domain RVs, $\Delta v_t$ is sufficient rather than using $v_t$.

Therefore, the goal of this work is two-fold: first we correct the systematic bias in RV; second, we provide relative RV measurement for the 92 342 time-domain

MRS stars. As a by-product, we give the constant star candidates (The constant stars here in this work represent the stars with low RV variations. They are not necessarily absolute constant stars, but may not show significant RV variation during the time-domain survey), which do not show significant RV shift in the MRS time-domain spectra.

This paper is organized as follows. The LAMOST MRS and the data are described in Section 2. The method of relative calibration is described in Section 3. The results are indicated in Section 4. The special cases are analyzed in Section 5. Finally, we summarize in Section 6.

## 2 DATA

The Guoshoujing Telescope (also known as LAMOST) is a 4-meter class reflecting Schmidt telescope with a 5-degree field-of-view. Totally 4000 fibers are installed at the 1.75 m-diameter large focal plane and 16 spectrographs, each of which accepts 250 fibers, are used to take spectra simultaneously. Each spectrograph contains two arms. For medium spectroscopic observation, the blue arm covers 4950–5350 Å and the red arm covers 6300–6800 Å with $R \sim 7500$.

As mentioned in Liu et al. (2020), the LAMOST MRS survey acquires observations in 14 bright and gray nights per month. A sky area of about 2000 square degrees, including various Galactic latitudes, is designed for the time-domain spectroscopic survey. It is expected that, after a 5-year MRS survey, there will be around 200 000 stars with $G < 14\,\mathrm{mag}$[1] to be observed multiple times.

The seeing, cloud coverage and checking of polluted light are evaluated to remove the low-quality observations from two-dimensional (2D) frames at first. Then the 2D medium-resolution frames are processed by the LAMOST 2D pipeline, which includes bias subtraction, fiber tracing, wavelength calibration, spectral extraction and sky subtraction. For an observation target, the spectra from the same night will be merged into a coadded spectrum, and the separate spectrum of each exposure is provided as well.

## 3 METHOD

The directly measured RV ($\widetilde{v}_{i,t}$) of a star $i$ observed at time $t$ is composed of the intrinsic RV ($v_{i,t}$), the systematic error ($\Delta u_t$) due to the wavelength calibration during the observation and the measurement uncertainty ($\epsilon_{i,t}$) induced during measurement, i.e.,

$$\widetilde{v}_{i,t} = v_{i,t} - \Delta u_t + \epsilon_{i,t}\,. \tag{1}$$
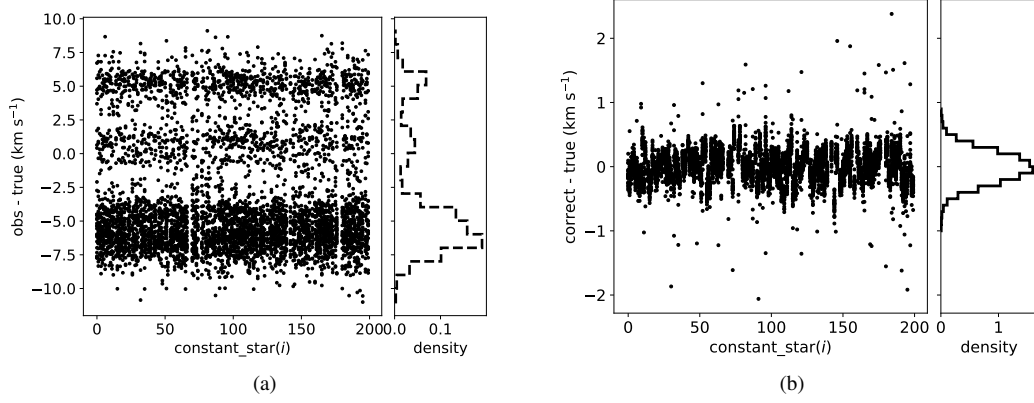
---

**Fig. 1** The result of mock stars. Panel (a) displays the distribution of the difference between the directly measured RVs and the ground truth velocities for mock constant stars. Panel (b) features the residual value between the corrected velocities and the ground truth velocities for mock constant stars.
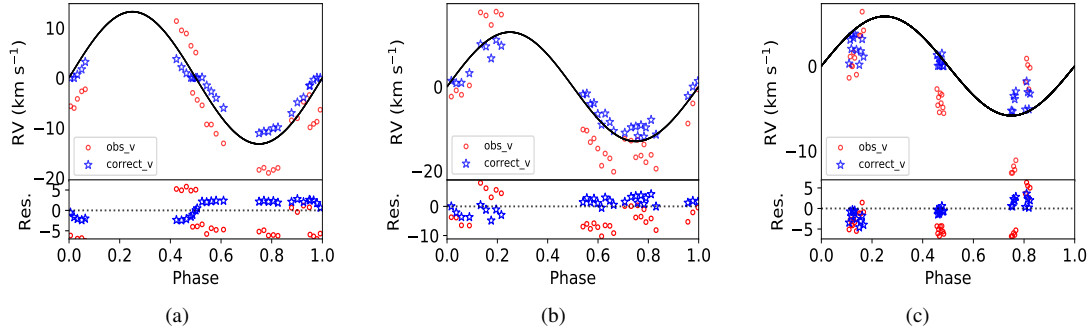


**Fig. 2** The velocity correction for three mock periodic variable stars with different velocity amplitudes. The *black-solid line* indicates the true RV curve. The *red circles* signify the directly measured RVs with shifts. The *blue stars* display the corrected RVs. The bottom panels feature the residual values with ground truth velocity of non-corrected and corrected velocities with *red circles* and *blue stars*, respectively.

**Table 1** The Detailed Parameters of Mock Binaries Shown in Fig. 2

| Panel | Period (d) | Velocity amplitude (km s$^{-1}$) | Inclination (°) | Eccentricity |
|-------|------------|----------------------------------|-----------------|--------------|
| (a) | 0.6894 | 13.23 | 88.65 | 0 |
| (b) | 0.6373 | 13.01 | 88.15 | 0 |
| (c) | 2.9098 | 5.91 | 81.79 | 0 |

In general, $v_{i,t}$ is independent of $t$. For a constant star, its RV does not change with observation time (i.e., $v_{i,t_1} = v_{i,t_2}$). When star $i$ is in a binary system or is a variable, $v_{i,t}$ changes periodically with $t$. For the former case, the relative RVs between two exposures should be around zero, while for the latter case, the differential RVs are sufficient for solving the velocity curve with higher precision than that derived from the absolutely calibrated RVs. Therefore, in this work, we only concentrate on the relative RV.

## 3.1 Relative Radial Velocity with Maximum Likelihood

We develop a likelihood method to measure the relative RV for a star from its medium-resolution spectra. First, each spectrum observed by LAMOST has to be normalized. We normalize each spectrum by dividing by its pseudo-continuum, and the pseudo-continuum is calculated as follows: each spectrum is fitted with a smoothing spline function iteratively, then the pixels with a value greater than the median value by 3 times the standard deviation are eliminated in each segmented wavelength (e.g. 100 Å). This process it iterated three times (Zhang et al. 2021).

Then, for the $i$th star with multiple exposures, we select the spectrum, denoted as $f_{\mathrm{ref},i}(\lambda)$, with highest signal-to-noise ratio (SNR) as the reference for the star. For the spectrum $f_{t,i}(\lambda, v)$, which is the spectrum of the $i$th star observed at time $t$, the likelihood distribution of the
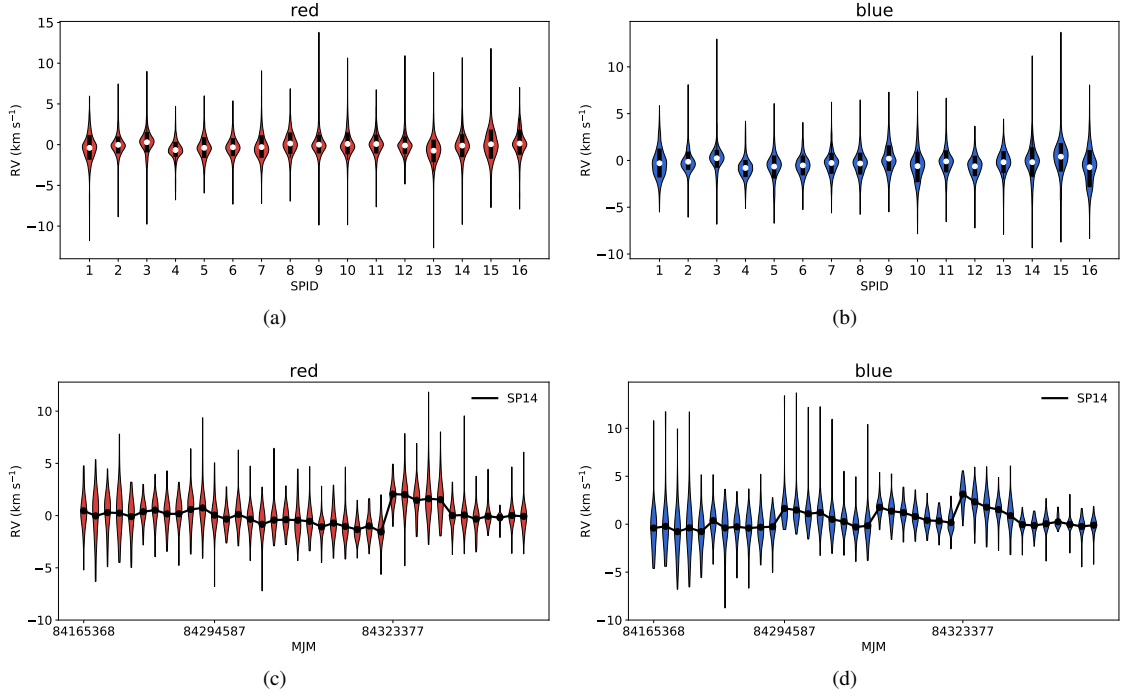
**Fig. 3** Panels (a) and (b) display the distribution of the directly measured relative RV from the spectra of constant star candidates from one sample field of LAMOST MRS in 16 spectrographs of red and blue arms. The *circles* are the mean relative RVs of candidate constant stars. Panels (c) and (d) feature the distribution of the directly measured relative RVs from the spectra observed by LAMOST MRS of constant star candidates for a spectrograph in red and blue arms, respectively, but in different exposures. The *black dots* indicate the initial mean RVs in different exposures.
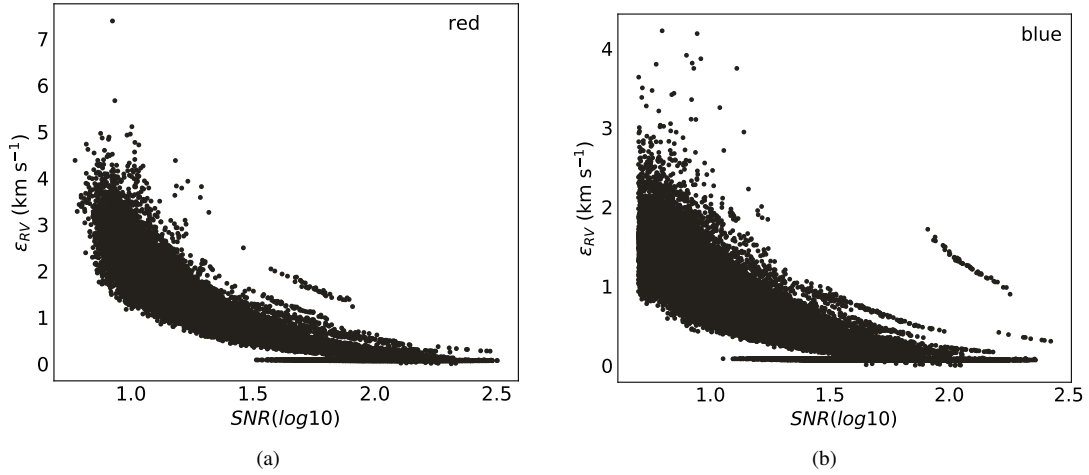


**Fig. 4** Panels (a) and (b) depict the relation between measurement uncertainty ($\epsilon_{RV}$) with SNR that is selected from the same sample field with Fig. 3 of LAMOST MRS in the red and blue arms, respectively.

relative RV $v$ is

$$p(v) = \prod_\lambda \frac{\exp[-\frac{(f_{t,i}(\lambda,v) - f_{ref,i}(\lambda))^2}{2(\sigma_{t,i}^2 + \sigma_{ref,i}^2)}]}{\sqrt{2\pi(\sigma_{t,i}^2 + \sigma_{ref,i}^2)}} \ , \qquad (2)$$

in which $\sigma_{t,i}$ and $\sigma_{ref,i}$ are the observational errors from the observed and reference spectra, respectively. In order to avoid the arithmetic errors caused by minimal values,

the logarithmic form as written below is actually used

$$\ln p(v) = \sum_\lambda [-\frac{(f_{t,i}(\lambda, v) - f_{ref,i}(\lambda))^2}{2(\sigma_{t,i}^2 + \sigma_{ref,i}^2)} \\ - 0.5 \ln(\sigma_{t,i}^2 + \sigma_{ref,i}^2) - 0.5 \ln 2\pi] \ . \qquad (3)$$
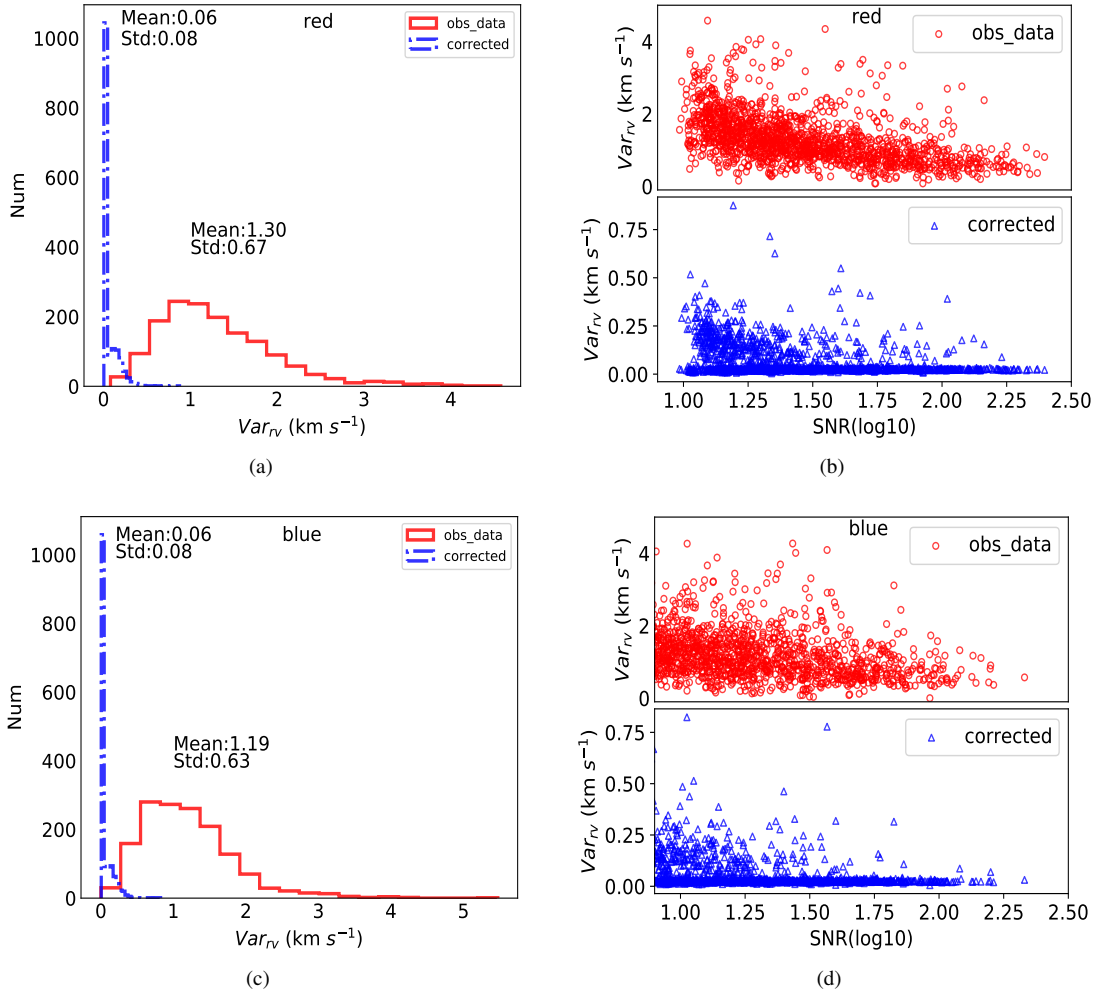
**Fig. 5** The non-calibrated and calibrated RV variation ($Var_{rv}$) from the same sample field with Fig. 3 of LAMOST MRS for selected candidate constant stars, and their relation with SNR for two arms. In panels (a) and (c) the *red solid* and *blue dash-dotted histograms* feature the $Var_{rv}$ distributions for constant stars with non-calibrated and calibrated data in the red and blue arm, respectively. In panels (b) and (d), the *red circles* and *blue triangles* correspond to the distributions of $Var_{rv}$ for constant stars with non-calibrated and calibrated data in the red and blue arms, respectively.

### 3.2 Calibrating Systematic Bias in Radial Velocity

In general, the wavelength calibration is based on an arc lamp, such as an Fe-Ar lamp. However, according to the tests, the wavelength calibration may suffer from a few km s$^{-1}$ systematic shift when comparing between different observations. In addition, the wavelength calibration of the red arm is more precise than the blue arm for LAMOST. In a few observation fields, RVs of constant stars obtained from high-resolution spectra can be used to further calibrate the wavelength in an absolute sense, since the precision of these RVs can be as high as a few hundred m s$^{-1}$ (see Huang et al. 2018). However, there are no high-resolution constant stars that have been identified in every LAMOST observation field. Therefore, we cannot only rely on the identified constant stars to improve the

velocity accuracy but require an approach in the manner of self-calibration.

Before we start the calibration process, we assume that the relative RVs of constant stars should be zero. The calibration process contains two steps in each iteration.

As the first step, we consider each star *i*. We calculate its relative RV variation over all exposures such as

$$\sigma_i^2 = \frac{1}{m} \sum_{t=1}^{m} (v_{i,t} - \bar{v}_i)^2 \,, \qquad (4)$$

where $v_{i,t}$ is the relative RV of star *i* in the *t*th observation, $\bar{v}_i$ the mean relative velocity over all exposures and *m* the number of exposures. For all stars observed by a spectrograph, the mean RV variation is $\bar{\sigma} = \sum_i \sigma_i / n$. The stars with $\sigma_i < \bar{\sigma}$ are selected as the candidate constant stars.

**Table 2** The Catalog of Relative Radial Velocity for LAMOST MRS Time-domain Plates

| ra | dec | hjd | SNR_r | DRV_r | DRV_r_err | DRV_r_corr | SNR_b | DRV_b | DRV_b_err | DRV_b_corr |
|---|---|---|---|---|---|---|---|---|---|---|
| 16.601013 | 3.819259 | 2458411.145602 | 24.34 | −4.25 | 1.05 | 0.04 | 15.32 | −4.90 | 0.72 | 0.02 |
| | | 2458416.177853 | 5.84 | −4.83 | 2.88 | 0.00 | 5.02 | −6.12 | 1.66 | 0.00 |
| | | 2458420.162413 | 15.43 | 0.51 | 1.56 | 0.03 | 9.21 | −0.26 | 1.06 | 0.00 |
| | | 2458449.087430 | 6.01 | −8.11 | 3.83 | 0.14 | 5.0 | −3.14 | 2.01 | 0.05 |
| | | ⋮ | ⋮ | ⋮ | ⋮ | ⋮ | ⋮ | ⋮ | ⋮ | ⋮ |
| 16.602702 | 4.362617 | 2458411.145607 | 7.95 | −4.40 | 3.21 | 0.05 | 6.06 | −7.05 | 1.83 | −0.83 |
| | | 2458439.058429 | 8.14 | 4.29 | 3.7 | 0.02 | 6.99 | −0.51 | 1.73 | 0.01 |
| | | 2458451.078222 | 11.4 | −1.95 | 2.86 | −0.03 | 10.9 | 0.06 | 1.24 | 0.01 |
| | | 2458453.050072 | 13.61 | 0.73 | 2.33 | 0.02 | 10.35 | 0.27 | 1.29 | −0.02 |
| | | ⋮ | ⋮ | ⋮ | ⋮ | ⋮ | ⋮ | ⋮ | ⋮ | ⋮ |
| 16.604269 | 5.121394 | 2458411.129353 | 42.14 | −3.37 | 0.51 | −0.02 | 21.26 | −3.77 | 0.37 | −0.01 |
| | | 2458420.112249 | 15.56 | 0.35 | 1.20 | −0.05 | 7.45 | −1.22 | 0.81 | −0.03 |
| | | 2458439.058448 | 22.54 | 0.95 | 0.83 | −0.03 | 11.16 | 0.83 | 0.58 | −0.01 |
| | | 2458451.061743 | 32.21 | −0.03 | 0.62 | 0.00 | 18.48 | −0.06 | 0.41 | −0.01 |
| | | ⋮ | ⋮ | ⋮ | ⋮ | ⋮ | ⋮ | ⋮ | ⋮ | ⋮ |
| 16.612777 | 2.792158 | 2458411.145590 | 16.02 | −6.16 | 1.57 | 0.05 | 5.82 | −11.03 | 1.28 | −0.83 |
| | | 2458439.058398 | 12.91 | −0.19 | 1.83 | 0.00 | 5.48 | −3.09 | 1.28 | 0.00 |
| | | ⋮ | ⋮ | ⋮ | ⋮ | ⋮ | ⋮ | ⋮ | ⋮ | ⋮ |
| ⋯ | ⋯ | ⋯ | ⋯ | ⋯ | ⋯ | ⋯ | ⋯ | ⋯ | ⋯ | ⋯ |

In the second step, we consider the velocities of stars in each exposure. We derive the mean relative velocities, denoted as $\bar{v}_t$, of the candidate constant stars selected from the first step in the $t$th exposure. Because the ground truth relative RV of constant stars should be zero, the non-zero $\bar{v}_t$ is mainly contributed by the systematic bias in wavelength calibration. Therefore, $\bar{v}_t$ is subtracted from $v_{i,t}$ for each star, including constant and non-constant stars. After subtraction, the candidate constant stars should be more concentrated around zero.

Note that as some contaminators may be introduced in the first step, we go back to step one and select the new candidate constant stars again with corrected relative RVs.

After a few iterations with the above two steps, when $\bar{v}_t$ tends to be very close to zero, and the variation of $\bar{v}_t$ for each exposure is lower than a predefined small threshold (we adopt any $|\bar{v}_t - \bar{v}_{t-1}| < 0.01 \, \text{km s}^{-1}$), the iteration is stopped.

### 3.3 Validation with Mock Stars

We rely on mock stars to quantitatively assess the performance of the calibration approach. We simulate the relative RV of the mock stars as the observation from one of the spectrographs. We produce 30 exposures in seven nights for these mock stars, including 200 constant stars with the ground truth velocity within $\pm 0.1 \, \text{km s}^{-1}$ with the measurement uncertainty in $0 \sim 2 \, \text{km s}^{-1}$, 10 non-constant stars with the RV changes of $2 \sim 10 \, \text{km s}^{-1}$ and 40 binary stars with the amplitude of $3 \sim 15 \, \text{km s}^{-1}$ in the period of $0.5 \sim 3$ d.

Then we add the systematic shift to these mock stars as the RV that is measured directly from the observation. The systematic shift of each night is randomly generated in the range of $-7 \sim 7 \, \text{km s}^{-1}$. In the mean time, a random error with a Gaussian error of $0.5 \, \text{km s}^{-1}$ is added to each exposure of the mock stars. After systematically shifting the RVs of the mock stars from zero, the constant stars' RV distribution becomes larger, and the difference between the observation and the ground truth velocity is depicted in Figure 1(a). The residual values between the corrected RVs and the ground truth velocities are plotted in panel (b). It is seen that the mean value of the residual velocities is essentially between $\pm 0.50 \, \text{km s}^{-1}$, except for non-constant stars.

In Figure 2, we display the velocity curves of three mock binary stars. The top panels in Figure 2 feature the velocity curves in black solid lines, the mock observed RVs are shown in red circles and the corrected velocities are marked in blue stars. The residual values are presented in the bottom panels of Figure 2, including the residual values between the mock observational RVs and the true velocity curves in red circles and the residual value between corrected velocities with the true velocity curves in blue stars. It is seen that the correction method can reconstruct well the RV curves of the binary stars. After correction, the residual values are smaller than before correction. The non-constant offset appearing in the residual panel of the figure is due to the fact that we have added a random RV measurement error to the simulation data (ranging from 0 to $2 \, \text{km s}^{-1}$). After correction of the systematic offset in
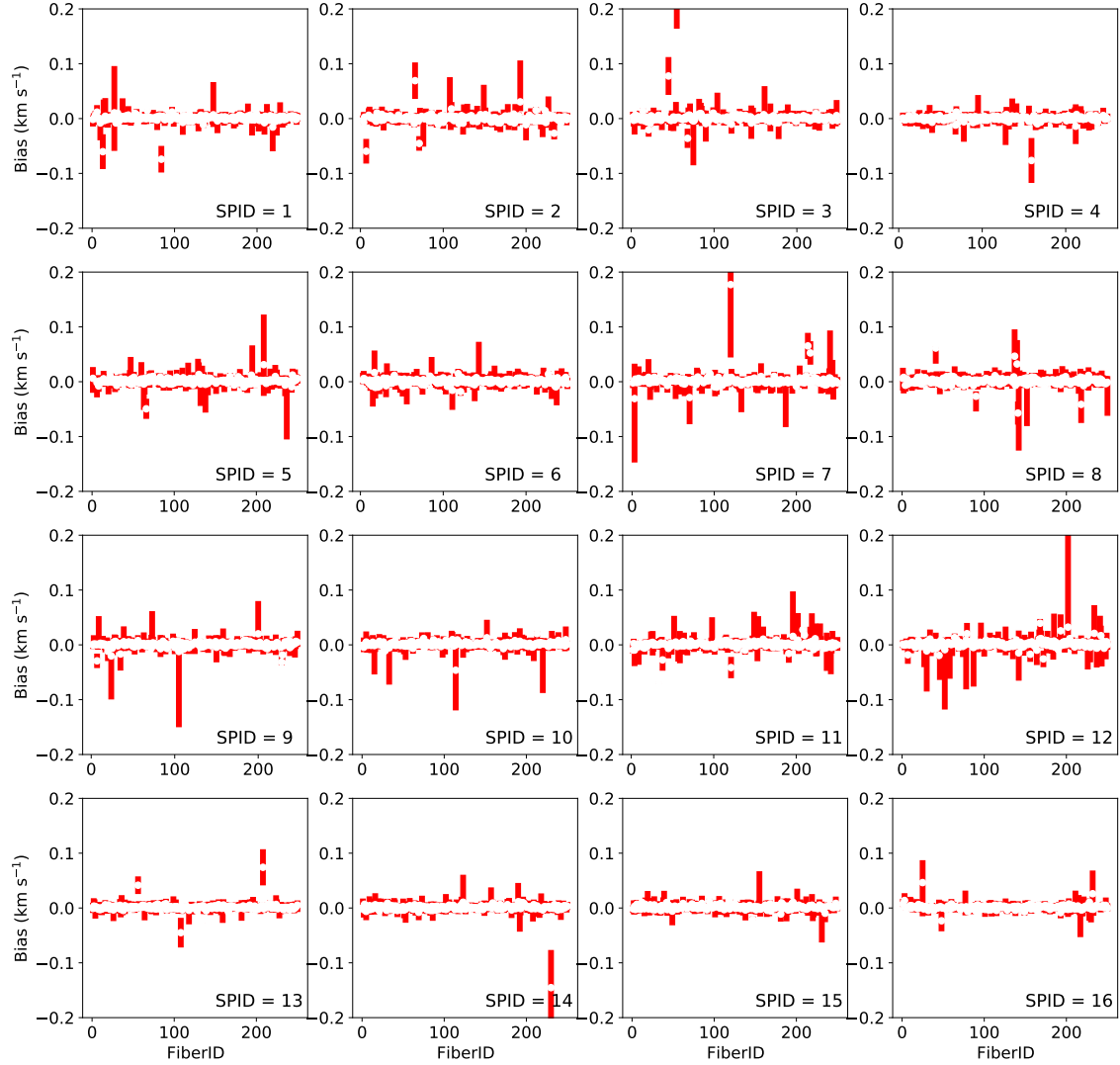
**Fig. 6** The RV bias due to fiber-to-fiber variations after calibration in the red arm.

each observation, the random error of RV added to the mock data still exists, leading to deviations larger than $\sim$ $0.5\,\mathrm{km\,s^{-1}}$, in the residuals. The detailed orbital parameters of the three mock binary stars are listed in Table 1.

## 4 RESULTS

We apply the approach of calibration based on relative RVs to the LAMOST MRS spectra with SNR larger than 5 that were made available in Data Release 7 (DR7) time-domain plate, approximately 2 215 918 spectra, including 1 170 445 from the red arm and 1 045 473 from the blue arm. Then we determined the relative RV in the red and blue arms separately. Each MRS spectrum is composed of two parts, the red covering from 6300 Å to 6800 Å and the blue covering from 4950 Å to 5350 Å. For measuring the relative RV, the wavelengths from 6400 Å to 6700 Å of the red arm are used, and the wavelengths from 5000 Å to 5300 Å from the blue arm are used. Then, the wavelength of each part of the spectrum is calibrated separately. The precision of wavelength calibration is better in the red than in blue, since the number of lamp spectral lines in the red part is more than that in the blue part. Meanwhile, the SNR of red spectra is in principle better than the blue arm due to larger throughput in the red part. Therefore, we measure the relative RV only using the red part spectra in the first step. Then we correct the relative RVs measured from the red part spectra. In the meantime, the candidate constant stars in each spectrograph are identified during the correction of RVs measured from spectra in the red part. Then, we directly utilize these candidate constant stars to correct the systematic shift induced in the wavelength calibration by spectra from the blue part.

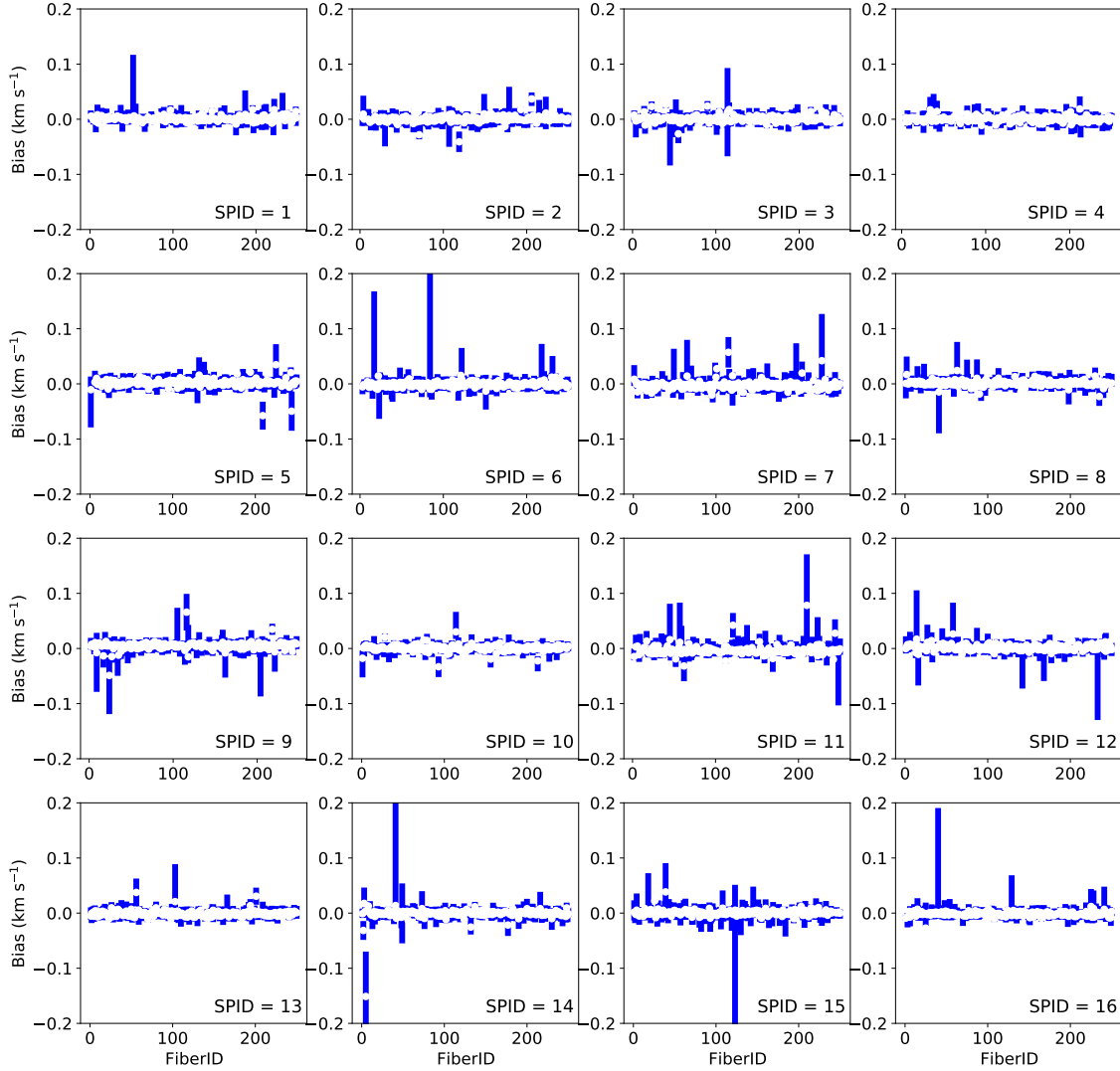Figure 3(a) and (b) displays the distribution of the directly measured relative RV from the spectra of constant

**Fig. 7** The RV bias due to fiber-to-fiber variations after calibration in the blue arm.

star candidates from one sample field of LAMOST MRS in 16 spectrographs of red and blue arms, respectively. The violin plot shows the dispersion of the relative RVs of constant star candidates in each spectrograph, and the white spots are the mean relative RVs of these constant star candidates in each spectrograph. It illustrates that the RV zero-points are slightly different between all spectrographs. Also, Figure 3(c) and (d) shows the relative RV distribution of constant star candidates for a spectrograph in 38 different exposures. The violin plot depicts the dispersion of the relative RVs of constant star candidates in each exposure, and the black dots are the mean relative RVs of these constant star candidates. It can be seen that the mean velocity of the candidate constant stars can move as much as $3\,\mathrm{km\,s^{-1}}$ from zero in some observations, especially in different nights. Moreover, according to panels (c) and (d), the variations of the mean

RVs of the red arm are more stable than those in the blue arm. To sum up, we perform calibration for each spectrograph separately, and apply the calibration on the red arm first.

Figure 4(a) and (b) depicts the relation between SNR with the measurement uncertainty of RV from the same sample field as Figure 3 of LAMOST MRS in the red and blue arms, respectively, and the measurement uncertainty of RV is calculated as the standard deviation of the best-fit Gaussian distribution corresponding to the likelihood function distribution, and defined as $\epsilon_{RV}$. Panels (a) and (b) both exhibit decreasing uncertainty of measurement with increasing SNR. The non-physical strips are found in Figure 4, which are caused by multi-star systems such as binaries. For these stars, the regular RV measurement method cannot identify the RV of their components correctly, resulting in a large measurement uncertainty for

some spectra with high SNR. It can also be seen that the uncertainty in measuring relative RV of the red arm is relatively larger than that of the blue arm due to the fact that $H_\alpha$ is usually the only prominent feature in the red arm, although it is more stable than the blue arm. So, we calibrate the systematic shift for red arm first, and the constant star candidates picked out after the red arm calibration are directly used in the blue arm. Utilizing these constant star candidates, the systematic shift of different exposures for the blue arm is then corrected.

Figure 5 features the distribution of non-calibrated and calibrated RV variation for candidate constant stars from the same sample field as Figure 3. The RV variation is measured by the standard deviation of the RVs of constant candidates over different exposures, defined as $Var_{rv}$. In addition, the relations between the RV variation of the two arms and SNR are also shown in Figure 5. Panel (a) displays the non-calibrated constant candidates' $Var_{rv}$ as a red solid histogram, with values that are directly measured from observational spectra in the red arm, representing the systematic shift of different exposures. The mean value of the non-calibrated variation is around 1.30 km s$^{-1}$. The calibrated $Var_{rv}$ of constant star candidates is represented as a blue dash-dotted histogram, which is tightly concentrated around zero. Panel (b) features the relation of the $Var_{rv}$ distribution and SNR of constant candidates, with the top panel showing the $Var_{rv}$ distribution for direct measurement from the observational spectra as red circles and the bottom displaying the $Var_{rv}$ distribution of constant candidates after calibration as blue triangles. After calibrating the systematic shift, the $Var_{rv}$ of constant stars is almost below 0.5 km s$^{-1}$. As panel (b) affirms, the calibration precision depends on the SNR, and the relatively lower precision results in high SNR because of the relatively large variation of SNR for the same target in time-domain observation. Panels (c) and (d) show similar distributions for blue arm calibration result with panels (a) and (b), respectively. In the blue arm, the initial constant candidates are adopted from the red arm correction result. Panel (c) displays the non-calibrated $Var_{rv}$ of the blue arm as a red histogram with a mean of 1.19 km s$^{-1}$, and the calibrated $Var_{rv}$ is shown as a blue dash-dotted histogram, which has mean $Var_{rv}$ of 0.06 km s$^{-1}$. Panel (d) also shows the decreasing $Var_{rv}$ of constant stars with increasing SNR, and after calibrating, the $Var_{rv}$ is almost below 0.5 km s$^{-1}$.

In total, 2 215 918 spectra from the 59 time-domain plates of LAMOST MRS survey of DR7 were calibrated in this work, including 1 170 445 of the red arm and 1 045 473 of the blue arm. The catalog of calibrated relative RV for these time-domain observations is listed in Table 2, including ra, dec, hjd, SNR, directly measured relative RV (DRV_r and DRV_b), the uncertainty of measurement (DRV_r_err and DRV_b_err), and the calibrated result (DRV_r_corr and DRV_b_corr). The "r" and "b" label the red and blue arms, respectively. The whole catalog is available in its entirety in machine-readable form.

After self-calibration in red and blue arms, we obtain 65 123 constant star candidates. The catalog of these constant star candidates is also available in machine-readable form. As the observations increase, these constant samples will evolve and become more accurate. This is a long-term process that can be followed for the LAMOST time-domain medium resolution survey.

Figure 6 and Figure 7 show typical RV variations for each fiber after calibration in the red and blue arms, respectively. The vertical red and blue lines indicate the range of the RV variations of constant stars for each fiber. It indicates that the mean value of RV variations due to the fiber-to-fiber changes is around 0 with a dispersion of 0.1 km s$^{-1}$, which corresponds to the limit of the calibration.

## 5 DISCUSSION

The precision of the calibration is highly correlated with the precision of the RV measurement method, and the measurement precision is limited by the spectral type and SNR. So, the precision of this relative RV measurement method is discussed in different types of spectra, as well as the pulsating variable stars and binary system.

We conducted the test for single line spectra at first, and we selected seven spectra with different types and high SNR (SNR>100) in LAMOST MRS. For these seven selected spectra, we simulated 1000 spectra at different SNR for each type. For each SNR, we randomly selected a spectrum as the template to measure their relative RV. The ground truth RV of these spectra should be zero. For the different types of spectra in the varying SNR, we obtained the standard deviation ($\sigma_{RV}$) from Monte Carlo simulation results as the measurement precision. Figure 8(a) and (b) demonstrates that the precision improves with increasing SNR in the red and blue arm, respectively. We infer from Figure 8 that there is a relatively low precision of types O, B and A when SNR is less than 40, especially in the blue arm (see panel (b)). For the types O, B and A, there are fewer lines to measure RV in the blue arm and the signal is mixed up with noise, so there is a relatively low precision of types O, B and A when SNR is less than 40 in the blue arm. This is improved a lot in the red arm, since the $H_\alpha$ line is dominant in the red arm. For types F, G, K and M, we can derive a more accurate RV in relatively high precision
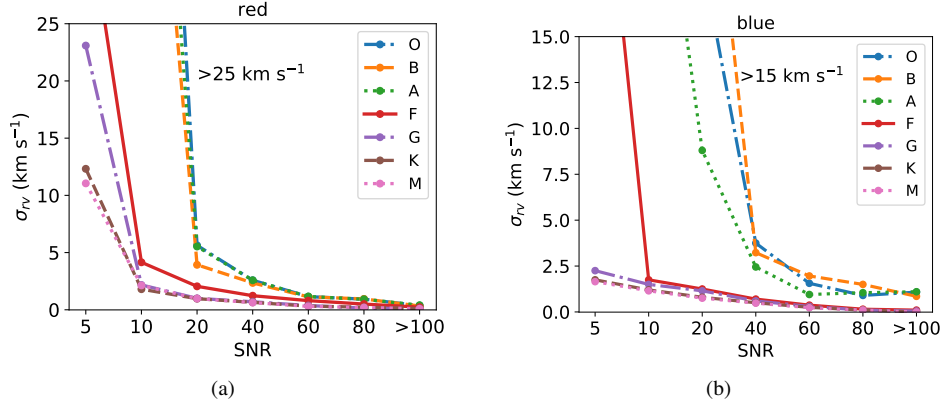
**Fig. 8** Panels (a) and (b) show the precision ($\sigma_{rV}$) of this relative RV measurement method for different types of spectra with different SNRs for the red and blue arms, respectively.
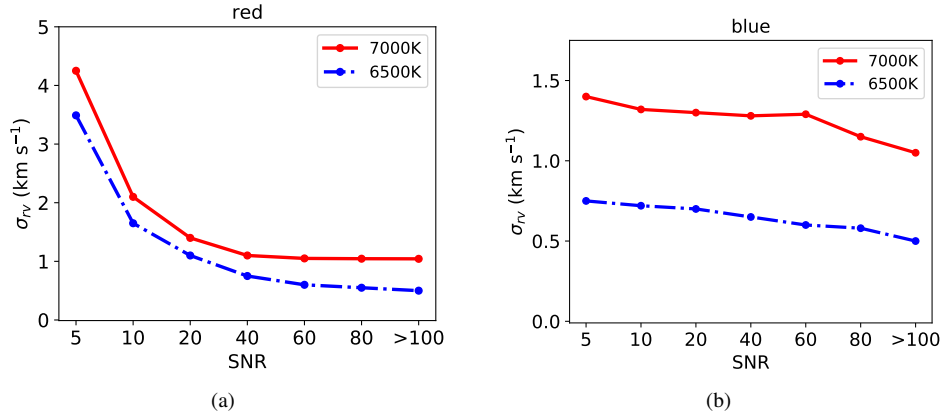


**Fig. 9** Panels (a) and (b) show the relative RV measurement precision ($\sigma_{rv}$) for the stars with large temperature change with different SNRs for red and blue arms, respectively.

even though they have a low SNR, because of their rich populations of spectral lines.

Then we test pulsating variable stars. As a pulsating variable star, its effective temperature, spectral features and RV may change in a short period, such as RR Lyrae. Because the periodic expansion and contraction of these stars cause a temperature change, and the luminosity also periodically increases and decreases, it appears that its brightness periodically brightened and darkened. It indicates that the spectra of the pulsating variable star may significantly change in a short period with its large changes in temperature.

So, we mimic pulsating variable star spectra by utilizing the standard template with different temperatures of 6000 K, 6500 K and 7000 K, with fixed metallicity of −1 dex and log*g* of 2.5 dex. We assume that the spectra in three temperatures are the observational spectra in the time-domain survey of an RR Lyrae star. We also produced 1000 mock spectra by the different SNR for the temperatures in 6500 K and 7000 K, and measured their

RV by comparing with the spectrum with temperature of 6000 K. Then we obtained the standard deviation from Monte Carlo simulation results as the measurement precision. Figure 9 shows $\sigma_{RV}$ in different temperatures with changing SNR in the red and blue arms. In Figure 9, the red solid line is the result of the temperature of 7000 K and the blue dash-dotted line is for the spectrum with 6500 K. It is seen that the precision is also increasing with increasing SNR and is relatively higher for a smaller temperature change. Figure 9 affirms that even though the pulsators change their temperature by 1000 K, the relative RVs are still reliable.

For the binary systems, we can derive the differential RV for single-line spectroscopic binary. But for a double-lined spectroscopic binary, we can derive the RV with this method only ift we can obtain both of the spectra at the time of eclipse and non-eclipse because the basic idea for this RV measurement method is to calculate the similarity for two spectra of the same target in different exposures. If the double-lined spectroscopic binary is always observed

at the time of non-eclipse, i.e. it shows a double-line in all exposures, the relative RV with assumption of a single star is no longer valid. So, for a double-lined spectroscopic binary, the differential RV cannot be measured accurately with this likelihood if the observational spectra are always double-lined. Their velocities should be dealt with in a different way but we can pick them out as variable stars. Therefore, in this paper, the double-lined binary stars are only marked and will be treated with another approach.

# 6 CONCLUSIONS

In this work, we mainly develop an approach in the manner of self-calibration by using differential RV for LAMOST time-domain medium resolution search, and it is practicable to correct systematic shift in different exposures by relying on the differential RVs. The precision of the RV zero-point for different exposures after correcting systematic shift can reach below $0.5\,\mathrm{km\,s^{-1}}$.

In total, 2 215 918 spectra from the 59 time-domain plates of LAMOST MRS of DR7 were calibrated in this work, including 1 170 445 of the red arm and 1 045 473 of the blue arm. The whole catalog of calibrated relative RVs of the spectra for the LAMOST time-domain medium resolution survey is provided in this paper. After self-calibration in red and blue arms, we obtain the 65 123 constant star candidates, whose RV variation reaches around zero after calibration. This self-calibration method can be utilized for the long-term observation of LAMOST time-domain medium resolution survey and can be relied on to select constant stars with a relatively high precision. These initial constant star candidates can provide a library of standard star candidates of RV for the LAMOST time-domain medium resolution search. As the observation time increases, the library of constant stars becomes more accurate. For scientific significance, the variable stars with a relatively small amplitude can be detected and their RVs are calibrated effectively by this self-calibration method.

# References

Arentoft, T., Grundahl, F., White, T. R., et al. 2019, A&A, 622, A190

Cropper, M., Katz, D., Sartoretti, P., et al. 2018, A&A, 616, A5

Cui, X.-Q., Zhao, Y.-H., Chu, Y.-Q., et al. 2012, RAA (Research in Astronomy and Astrophysics), 12, 1197

De Silva, G. M., Freeman, K. C., Bland-Hawthorn, J., et al. 2015, MNRAS, 449, 2604

Deng, L.-C., Newberg, H. J., Liu, C., et al. 2012, RAA (Research in Astronomy and Astrophysics), 12, 735

Gaia Collaboration, Prusti, T., de Bruijne, J. H. J., et al. 2016, A&A, 595, A1

Gao, H., Zhang, H.-W., Xiang, M.-S., et al. 2015, RAA (Research in Astronomy and Astrophysics), 15, 2204

Gao, S., Liu, C., Zhang, X., et al. 2014, ApJL, 788, L37

Gilmore, G., Randich, S., Asplund, M., et al. 2012, The Messenger, 147, 25

Huang, Y., Liu, X.-W., Chen, B.-Q., et al. 2018, AJ, 156, 90

Katz, D., Munari, U., Cropper, M., et al. 2004, MNRAS, 354, 1223

Liu, C., Fu, J., Shi, J., et al. 2020, arXiv e-prints, arXiv:2005.07210

Liu, J., Zhang, H., Howard, A. W., et al. 2019, Nature, 575, 618

Luo, A. L., Zhao, Y.-H., Zhao, G., et al. 2015, RAA (Research in Astronomy and Astrophysics), 15, 1095

Majewski, S. R., Schiavon, R. P., Frinchaboy, P. M., et al. 2017, AJ, 154, 94

Mesa, V., Alonso, S., Coldwell, G., Lambas, D. G., & Nilo Castellon, J. L. 2021, MNRAS, 501, 1046

Pang, X., Li, Y., Yu, Z., et al. 2021a, ApJ, 912, 162

Pang, X., Yu, Z., Tang, S.-Y., et al. 2021b, arXiv e-prints, arXiv:2106.07658

Sana, H., de Mink, S. E., de Koter, A., et al. 2012, Science, 337, 444

Sana, H., de Koter, A., de Mink, S. E., et al. 2013, A&A, 550, A107

Steinmetz, M., Zwitter, T., Siebert, A., et al. 2006, AJ, 132, 1645

Steinmetz, M., Guiglion, G., McMillan, P. J., et al. 2020, AJ, 160, 83

Tian, H., Liu, C., Wang, Y., et al. 2020, ApJ, 899, 110

Tian, Z.-J., Liu, X.-W., Yuan, H.-B., et al. 2018, RAA (Research in Astronomy and Astrophysics), 18, 052

Wang, R., Luo, A. L., Chen, J. J., et al. 2019, arXiv e-prints, arXiv:1908.04773

Wu, Y., Du, B., Luo, A., Zhao, Y., & Yuan, H. 2014, in Statistical Challenges in 21st Century Cosmology, eds. A. Heavens, J.-L. Starck, & A. Krone-Martins, 306, 340

Yanny, B., Rockosi, C., Newberg, H. J., et al. 2009, AJ, 137, 4377

Zhang, B., Li, J., Yang, F., et al. 2021, arXiv e-prints, arXiv:2105.11624

Zhao, G., Zhao, Y.-H., Chu, Y.-Q., et al. 2012, RAA (Research in Astronomy and Astrophysics), 12, 723